



Effects of crystalline growth on structural and luminescence properties of $\text{Ca}_{10-3x}\text{Eu}_{2x}(\text{PO}_4)_6\text{F}_2$ nanoparticles fabricated by using microwave driven hydrothermal process

Katarzyna Zawisza, Paulina Sobierajska, Guillaume Renaudin, Jean-Marie Nedelec, Rafael Wiglusz

► To cite this version:

Katarzyna Zawisza, Paulina Sobierajska, Guillaume Renaudin, Jean-Marie Nedelec, Rafael Wiglusz. Effects of crystalline growth on structural and luminescence properties of $\text{Ca}_{10-3x}\text{Eu}_{2x}(\text{PO}_4)_6\text{F}_2$ nanoparticles fabricated by using microwave driven hydrothermal process. CrystEngComm, 2017, 10.1039/C7CE01454F . hal-01613312

HAL Id: hal-01613312

<https://hal.science/hal-01613312>

Submitted on 9 Oct 2017

HAL is a multi-disciplinary open access archive for the deposit and dissemination of scientific research documents, whether they are published or not. The documents may come from teaching and research institutions in France or abroad, or from public or private research centers.

L'archive ouverte pluridisciplinaire **HAL**, est destinée au dépôt et à la diffusion de documents scientifiques de niveau recherche, publiés ou non, émanant des établissements d'enseignement et de recherche français ou étrangers, des laboratoires publics ou privés.

CrystEngComm

Accepted Manuscript



This article can be cited before page numbers have been issued, to do this please use: R. J. Wiglusz, K. Zawisza, P. Sobierajska, G. Renaudin and J. Nedelec, *CrystEngComm*, 2017, DOI: 10.1039/C7CE01454F.



This is an Accepted Manuscript, which has been through the Royal Society of Chemistry peer review process and has been accepted for publication.

Accepted Manuscripts are published online shortly after acceptance, before technical editing, formatting and proof reading. Using this free service, authors can make their results available to the community, in citable form, before we publish the edited article. We will replace this Accepted Manuscript with the edited and formatted Advance Article as soon as it is available.

You can find more information about Accepted Manuscripts in the [author guidelines](#).

Please note that technical editing may introduce minor changes to the text and/or graphics, which may alter content. The journal's standard [Terms & Conditions](#) and the ethical guidelines, outlined in our [author and reviewer resource centre](#), still apply. In no event shall the Royal Society of Chemistry be held responsible for any errors or omissions in this Accepted Manuscript or any consequences arising from the use of any information it contains.

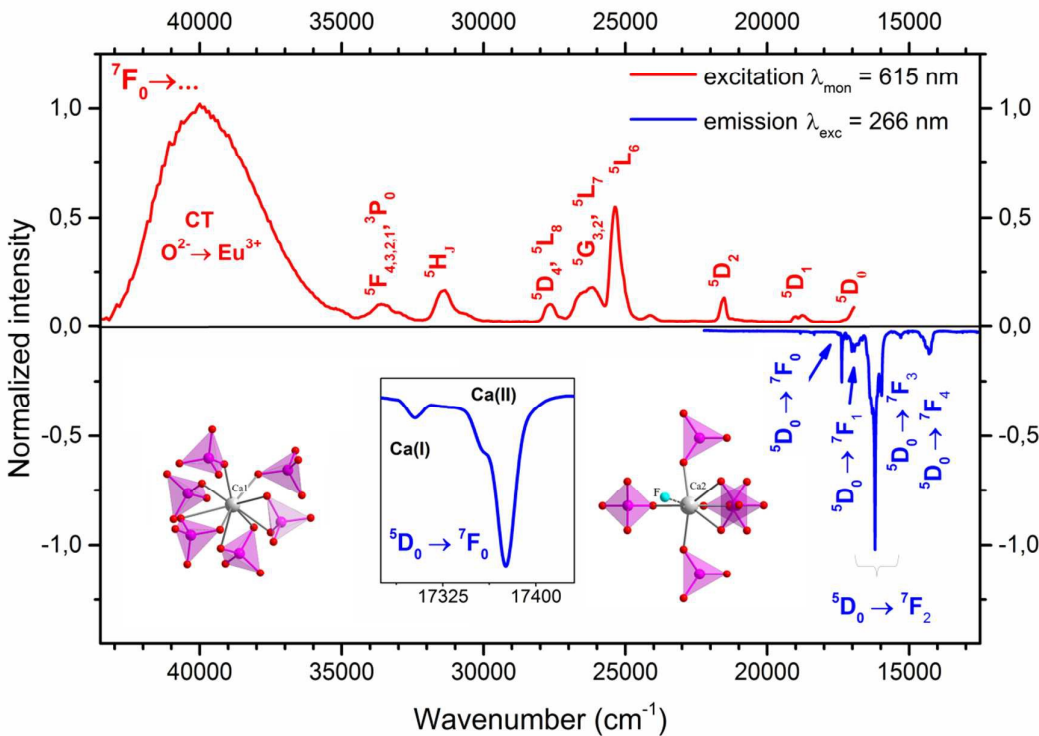
Effects of crystalline growth on structural and luminescence properties of $\text{Ca}_{(10-3x)}\text{Eu}_{2x}(\text{PO}_4)_6\text{F}_2$ nanoparticles fabricated by using microwave driven hydrothermal process

Katarzyna Zawisza^{1*}, Paulina Sobierajska¹, Guillaume Renaudin², Jean-Marie Nedelec² and Rafal J. Wiglusz^{1*}

¹Institute of Low Temperature and Structure Research, PAS, Okolna 2, 50-422 Wrocław

²Université Clermont Auvergne, CNRS, SIGMA Clermont, ICCF, F-63000 Clermont-Ferrand, France

*Corresponding author: R.Wiglusz@int.pan.wroc.pl and K.Zawisza@int.pan.wroc.pl



The Eu^{3+} doped fluorapatite nanopowders were synthesized by microwave assisted hydrothermal technique and annealed in the 500 – 1000°C temperature range for 3 h.

Effects of crystalline growth on structural and luminescence properties of $\text{Ca}_{(10-3x)}\text{Eu}_{2x}(\text{PO}_4)_6\text{F}_2$ nanoparticles fabricated by using microwave driven hydrothermal process

Katarzyna Zawisza^{1*}, Paulina Sobierajska¹, Guillaume Renaudin², Jean-Marie Nedelec² and Rafal J. Wiglusz^{1*}

¹*Institute of Low Temperature and Structure Research, PAS, Okolna 2, 50-422 Wrocław*

²*Université Clermont Auvergne, CNRS, SIGMA Clermont, ICCF, F-63000 Clermont-Ferrand, France*

Abstract

The Eu^{3+} doped fluorapatite nanopowders were synthesized by microwave assisted hydrothermal technique and annealed in the 500 – 1000°C temperature range for 3 h. The europium ions concentration was determined to be in the 0.5 – 10 mol% concentration range. The morphology and structural properties of $\text{Ca}_{(10-3x)}\text{Eu}_{2x}(\text{PO}_4)_6\text{F}_2$ were determined by using TEM (Transmission Electron Microscopy), XRPD (X-Ray Powder Diffraction) techniques as well as the IR (Infrared) and Raman spectroscopy. The average nanoparticle sizes were calculated by Rietveld refinement being in the range from 30 nm for as-prepared samples to above 100 nm for materials thermally treated at 1000°C. The particles have grown up in rectangular prism nanorods. The spectroscopic properties of obtained materials were observed to be dependent on the dopant concentration and annealing temperature and were studied in details. The Judd-Ofelt theory was applied and correlated with structural and optical properties to get detailed insight into fluorapatite structures.

Keywords: calcium fluorapatite, europium doping, photoluminescence, spectroscopy, luminescence, europium ions, phosphate, nanocrystalline apatite, nanopowder

*Corresponding author:

E-mail: R.Wiglusz@int.pan.wroc.pl and K.Zawisza@int.pan.wroc.pl

Phone: +48-71-395-41-59

Fax: +48-71-344-10-29

Homepage address www.intibs.pl

1. Introduction

The apatite is a large family of compounds widespread in nature. The most ideal representative of it is calcium hydroxyapatite ($\text{Ca}_{10}(\text{PO}_4)_6(\text{OH})_2$ – hereafter CaHAp), which can be easily substituted by different ions¹. Nowadays apatites are extensively applied in many industrial fields as catalysts, laser hosts, luminescent materials, gas sensors, ionic conductors and adsorbants^{2–5}. Additionally, these calcium phosphates play an important role as a material for biological applications due to their excellent biological properties. Synthetic apatites are highly similar to biological inorganic matrix of hard tissues in vertebrates and they are characterized by good biocompatibility, osteoconductivity, non-toxicity, non-immunogenicity and bioactivity as the ability to induce the formation of a direct chemical bond with living tissues^{1,6,7}. An innovative approach in advanced biomaterials is focused on substances containing elements that are integral components of living system. Since, calcium and phosphorus are main constituents of hard tissue, the calcium phosphate family has caught the attention as fundamental compounds for this goal. According to these numerous advantages this material is widely used and implanted to repair damaged bones and as teeth and bones fillers^{8,9}.

It is expected that the presence of fluorine ions in the apatite structure is enhancing the physical and biological properties comparatively to hydroxyapatite⁸. Synthetic fluorapatite ($\text{Ca}_{10}(\text{PO}_4)_6\text{F}_2$ – hereafter CaFAp) is harder, stiffer, possesses better chemical and thermal stability, higher acid resistance, lower solubility in water compared to CaHAp¹⁰. It is known that fluorine ions release from CaFAp could lead to inhibition of bacteria metabolism¹¹. According to this, F^- ions prevent and control dental caries, stimulate bone cells proliferation and differentiation¹². Furthermore, this essential microelement is necessary for the normal dental and bone formation in living systems^{13,14}. In response to the consumption of fluorinated water CaFAp is formed on the outer layer of the tooth¹⁵. *In vitro* studies have confirmed biocompatibility of calcium fluorapatite and have shown release of F^- ions in a controlled rate. Moreover, it has been demonstrated that it exhibits integration with hard tissue and longer resorption time than ordinary CaHAp^{12,13,15}. Due to these advantages fluorapatite is considered as a biological material and as a fluorescence bioprobe for bio-imaging and biosensing.

Fluorapatite crystallizes in hexagonal space group $P6_3/m$ (No. 176) with unit cell formula $\text{Ca}_{10}(\text{PO}_4)_6\text{F}_2$, which contains ten calcium cations in two nonequivalent sites. There is four Ca(1) ions with nine-fold C_3 symmetry (Wyckoff position 4f, coordinates $[1/3, 2/3, z]$), each surrounded by nine oxygen atoms, and six Ca(2) ions with seven-fold C_2 symmetry (Wyckoff position 6h, coordinates $[x, y, 1/4]$), each coordinated by six oxygen atoms and one fluoride atom. Rare earth ions can locate in both calcium sites depending on local charge compensation^{16,17}. The F^- ion has smaller size (1.28 Å) than OH^- (1.37 Å) hence fluorine ions pack closely which results in smaller cell volume¹⁰. The success of rare-earth doping is expected in view of similarity in ionic radius of lanthanide ions and calcium ion and high affinity to PO_4^{3-} . Moreover, it is important to note that substitution of OH^- groups by F^- ions could contribute to the enhancement of luminescence efficiency¹⁸. The presence of OH^- groups in matrix leads to strong non-radiative energy migration caused by coupling between lanthanide ions and OH^- vibrations¹⁹. Materials containing fluorine ions are characterized by low phonon energy¹⁸.

The optical properties of the fluorapatites doped with rare earth ions such as $\text{Nd}^{3+20-22}$, Pr^{3+23} , Tm^{3+24} , $\text{Eu}^{3+16,17,25,26}$, $\text{Yb}^{3+}/\text{Ho}^{3+18,27}$, $\text{Er}^{3+}/\text{Yb}^{3+28}$ have been studied. These investigation were concerning mostly polycrystalline powders and single crystals as phosphors and laser hosts.

2. Experimental

2.1. Synthesis of $\text{Ca}_{10}(\text{PO}_4)_6\text{F}_2:\text{Eu}^{3+}$ nanoparticles

The nanocrystalline powders of fluorapatite doped with Eu^{3+} ions were prepared by microwave stimulated hydrothermal method. Concentration of the europium(III) ions has been set to 0.5, 1, 2, 3, 5, 10 mol% in proportion to the overall molar content of Ca^{2+} ions. As starting substrates have been used analytical grade of $\text{Ca}(\text{NO}_3)_2 \cdot 4\text{H}_2\text{O}$ (99+% Acros Organics), $\text{NH}_4\text{H}_2\text{PO}_4$ (99.995% Alfa Aesar), NH_4F (98% Alfa Aesar), Eu_2O_3 (99.99% Alfa Aesar) and $\text{NH}_3 \cdot \text{H}_2\text{O}$ (99% Avantor Poland) for pH adjustment. At first, the stoichiometric amounts of Eu_2O_3 were digested in an excess of the HNO_3 (ultrapure Avantor Poland) to obtain water soluble nitrates and then europium(III) nitrates were re-crystallized three times. Subsequently, calcium nitrate was dissolved in deionized water together with europium nitrate. The suitable amount of ammonium phosphate dibasic and then ammonium fluoride were added to the mixture leading to fast precipitation of the by-product. The pH of the

dispersion was modulated to 10 by adding ammonia, transferred into the Teflon vessel and set in the microwave reactor (ERTEC MV 02-02). After 90 min of the microwave stimulated hydrothermal processing at 280°C and under autogenous pressure of 60 atm., a nanocrystalline powder was obtained. Powder was washed with de-ionized water several times and dried at 70°C for 24 h in order to get the final product. In order to receive well-crystallized product and get rid of residual amorphous phase thermal treatment in the temperature range of 500-1000°C was applied.

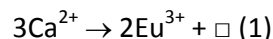
2.2. Characterization

The X-ray powder diffraction (XPRD) patterns were measured in the 3-120° 2 θ range by using an X'Pert Pro PANalytical X-ray diffractometer equipped with Ni-filtered Cu $K\alpha_1$ radiation ($K\alpha_1 = 1.54060 \text{ \AA}$, $V = 40 \text{ kV}$, $I = 30 \text{ mA}$). The experimental XRD patterns were compared with the standard from Inorganic Crystal Structure Database (ICSD) and analyzed. The microstructure and morphology of synthesized nanofluorapatites were investigated by High Resolution Transmission Electron Microscopy (HRTEM) using Philips CM-20 SuperTwin microscope, operating at 200 kV. Specimen for HRTEM was set up by dispersing a small amount of sample in methanol and putting a droplet of the suspension on a copper microscope grid covered with perforated carbon.

The IR measurements were performed at 295 K in KBr pellets using the FT-IR Biorad 575C spectrometer in the range of 3800-400 cm^{-1} . Raman spectra were measured using a Bruker FT 100/S spectrometer with YAG:Nd laser excitation (1064 nm). Both IR and Raman spectra were recorded with a spectral resolution of 2 cm^{-1} .

The Rietveld refinements of X-ray powder patterns were performed for each sample with the program FullProf.2k²⁹ and Maud 2.68 software³⁰. The used procedure (both data-collection and refinement strategy) corresponded to the general guidelines for structure refinement using the Rietveld method (whole-profile) formulated by the International Union of Crystallography Commission on Powder Diffraction^{31,32}. The initial structural parameters of fluorapatite, $\text{Ca}_{10}(\text{PO}_4)_6\text{F}_2$, were taken from³³: space group $P6_3/m$, $Z = 1$, $a = 9.363 \text{ \AA}$ and $c = 6.878 \text{ \AA}$, 7 independent atomic positions: two Ca positions in sites $4f$ ($z = 0.0012$) and $6h$ ($x = 0.2415$, $y = 0.0071$), one P position in site $6h$ ($x = 0.3982$, $y = 0.3689$), and three O positions in sites $6h$ ($x = 0.3268$, $y = 0.4850$ and $x = 0.5881$, $y = 0.4668$), $12i$ ($x = 0.3415$, $y = 0.2569$, $z = 0.0704$) and one F position in site $2a$. Eu^{3+} cations were allowed to substitute Ca^{2+}

cation in the two Ca(1) and Ca(2) calcium sites by considering the following vacancy mechanism:



The initial structural parameters of europium phosphate phases were taken from literature for EuPO_4 monazite³⁴ and for Eu_3PO_7 (isostructural to Nd_3PO_7)³⁵.

The excitation spectra were measured using FLS980 Fluorescence Spectrometer from Edinburgh Instruments equipped with 450 W Xenon lamp. The excitation of 300 mm focal length monochromator was in Czerny-Turner configuration. The excitation arm was supplied with holographic grating of 1800 lines/mm grating blazed at 250 nm. The luminescence spectra were recorded using Jobin-Yvon THR1000 monochromator equipped with Hamamatsu R928 photomultiplier and 1200 lines/mm grating blazed at 500 nm. As an excitation source the third harmonic of a pulsed YAG:Nd laser ($\lambda_{\text{exc}} = 266$ nm) was used. The spectral resolution was 0.1 nm. All the emission and excitation spectra were respectively corrected to the detector sensitivity and excitation source intensity.

The luminescence kinetics measurements were performed using Jobin-YvonTHR1000 monochromator equipped with R928 Hamamatsu photomultiplier using as the excitation source pulsed YAG:Nd laser (3rd harmonic, $\lambda_{\text{exc}} = 266$ nm). The decay profiles were collected using a LeCroy WaveSurfer 400 MHz oscilloscope. The decay curve fitting was performed with the help of Origin 9.1 software.

3. Results and Discussion

3.1. Structure and morphology analysis

The formation of the $\text{Ca}_{(10-3x)}\text{Eu}_{2x}(\text{PO}_4)_6\text{F}_2$ nanocrystals doped with $2x$ Eu^{3+} ions (where $2x = 0.5, 1, 2, 3, 5, 10$ mol%) were observed by the XRD measurement as a function of optical ions concentration and annealing temperatures 600°, 800° and 1000°C (see Figures 1 and s1). All materials synthesised by hydrothermal procedure presented detectable crystallinity at entire range of applied post-heat treatment temperatures (as-synthesised – 1000°C/3h). As can be seen, pure hexagonal phases corresponding to the reference standard of the $\text{Ca}_{10}(\text{PO}_4)_6\text{F}_2$ (ICSD – 9444³³) are observed for samples doped up to 3 mol% of Eu^{3+} ions and annealed up to 900°C. Above terminal concentration of 3 mol%, one can observed phases separation due to the limited solubility of europium(III) ions in fluorapatite and appearance of extra EuPO_4 at around $2\theta = 29^\circ$. Above post-heat treatment temperature of 900°C, it is

observed an occurrence of additional $\text{Ca}_3(\text{PO}_4)_2$ phase due to escaping of fluorine ions and dehydration process of fluorapatite. All samples heat-treated at 1000°C contained $\text{Ca}_3(\text{PO}_4)_2$ phase.

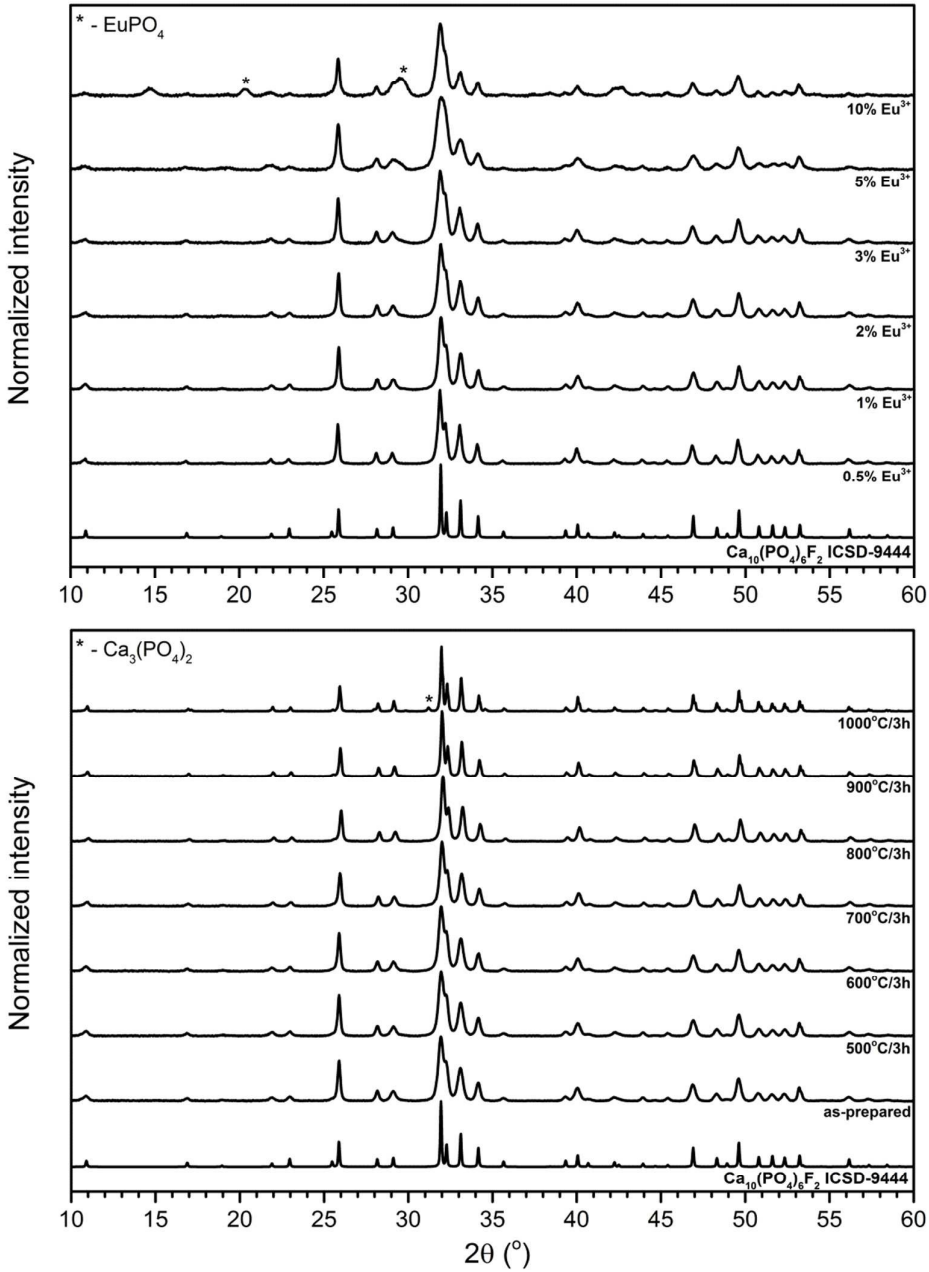


Figure 1. X-ray powder diffraction patterns of the $\text{Ca}_{(10-3x)}\text{Eu}_{2x}(\text{PO}_4)_6\text{F}_2$ annealed at $600^\circ\text{C}/3\text{h}$ depending on optical ions concentration (upper) and the $\text{Ca}_{9.85}\text{Eu}_{0.1}(\text{PO}_4)_6\text{F}_2$ depending on annealed temperature.

The quality of structural Rietveld refinement was checked by R -values to detect the consistency with a hexagonal structure. However, a difference in the observed and

calculated patterns is the best method to evaluate the Rietveld refinement. Moreover, other parameters with additional functions were applied to find a structural refinement with better quality and reliability. As can be seen, Figure 2 shows a good agreement between the observed XRD pattern and the theoretical fit calculation for $\text{Ca}_{9.85}\text{Eu}_{0.1}(\text{PO}_4)_6\text{F}_2$ obtained at 500°C which implicate the success of the Rietveld refinement method as displayed by the small differences of the ($Y_{\text{Obs}} - Y_{\text{Calc}}$) intensity. The base lines during this method were used. The projection of the unit cell with the indication of the coordination polyhedra are presented in Figure 3 whereas results of calculations are given in Table 1.

Table 1. Unit cell parameters (a , c), cell volume (V), grain size as well as refine factor (R_w) for the $\text{Ca}_{(10-3x)}\text{Eu}_{2x}(\text{PO}_4)_6\text{F}_2$ prepared at different temperatures calculated by Maud 2.68 software.

Sample		a (Å)	c (Å)	V (Å ³)	size [nm]	R_w (%)
single crystal ³⁶		9.480(0)	6.900(0)	537.02(7)	–	–
600°C	0.5 %	9.388(4)	6.895(1)	526.32(5)	41.15	2.0
	1 %	9.374(8)	6.886(1)	524.11(7)	36.51	1.7
	2 %	9.377(9)	6.888(0)	524.60(8)	30.86	1.5
	3 %	9.386(0)	6.892(0)	525.82(0)	27.23	1.4
800°C	0.5 %	9.366(3)	6.878(4)	522.58(2)	67.23	2.1
	1 %	9.352(5)	6.870(3)	520.42(9)	47.94	2.5
	2 %	9.364(5)	6.877(9)	522.34(3)	50.00	3.0
	3 %	9.356(4)	6.871(3)	520.93(9)	44.39	2.8
1000°C	0.5 %	9.363(0)	6.873(1)	521.81(1)	168.39	2.9
	1 %	9.368(2)	6.878(4)	522.79(4)	146.65	3.2
	2 %	9.347(7)	6.866(0)	519.57(0)	118.91	3.1
	3 %	9.363(1)	6.875(0)	521.96(6)	138.78	3.0
1% Eu ³⁺	as-prepared	9.381(6)	6.887(3)	524.97(0)	32.70	1.9
	500°	9.375(8)	6.886(3)	524.24(4)	35.65	2.1
	600°	9.374(8)	6.886(1)	524.11(7)	36.51	1.7
	700°	9.363(8)	6.878(2)	522.28(8)	39.38	2.2
	800°	9.352(5)	6.870(3)	520.42(9)	47.94	2.5
	900°	9.361(0)	6.874(3)	521.67(9)	89.39	2.8
	1000°	9.368(2)	6.878(4)	522.79(4)	146.65	3.2

The general trend has been observed that all unit cell parameters decrease with an increase in the annealing temperature or otherwise, with an increase in the particle size. Lower unit cell parameters were observed for all nanopowders compared to the $\text{Ca}_{10}(\text{PO}_4)_6\text{F}_2$ single crystal, as a result of the so-called particle size effect. The totally refined amount of europium, considering the substituted ions into the CaFAp and the Eu^{3+} ions from additional europium phosphates, is closely correlated to the europium amount incorporated into the matrix during the synthesis. Two samples were slightly deviating from the targeted values of Eu^{3+} ions concentration: $2x = 3\%$ and $2x = 2\%$ for the thermal treatment at 800°C (see Figure s2). The lack of refined Eu^{3+} ions amount could be attributed to a small amount of EuPO_4 phase (less than 1 wt % of monazite would be enough to reach the targeted value). Up to $2x = 2\%$, samples are single phase whatever the temperature of the heat treatment. For $2x = 3\%$, samples are still single phase except for the higher thermal temperature of 1000°C . For higher $2x$ values 5% and 10%, all samples contain monazite as secondary phase (between 3 and 10 weight percent, see Figure s3). And for the $2x = 10\%$ sample heat treated at 1000°C a third Eu_3PO_7 phase is also present. Clearly, these observations indicate that: 1/ the calcium to europium substitution is limited to a maximal value around 4% in CaFAp, 2/ the higher is the thermal treatment, the lower is this substitution level. The unit cell volume is not so much affected by the calcium to europium substitution. Nevertheless, the general trend can be extracted from the unit cell volume variation associated to the thermal treatment: the first moderate heat treatment at 500°C induces shrinkage of the unit cell volume and the following 800°C and 1000°C heat treatment show an increase of the unit cell volume. A heat treatment of 1000°C is needed to exceed the level observed for the as-prepared samples. The a lattice parameter evolutions are similar to those of the unit cell volume. The c lattice parameter evolutions are somehow different: the c lattice parameter is slightly decreasing with increasing in heat treatment temperature, and the Eu^{3+} ions substitution is becoming dependent on heat treatment: the higher is the calcium to europium substitution, the smaller is the c lattice parameter after heat treatment (see Table 1). This observation seems to indicate that the location of the Eu^{3+} ions (either Ca(1) or Ca(2) site) is temperature dependent. For comparison, the following ionic radii can be found: Ca^{2+} 1.06 Å and Eu^{3+} 1.01 Å for a seven-fold coordination (Ca(2) site), and Ca^{2+} 1.18 Å and Eu^{3+} 1.12 Å for a nine-fold coordination (Ca(1) site)³⁷. So the Eu^{3+} ion is slightly smaller than Ca^{2+} cation. The x refined values for the as-prepared series are in very good agreement with the targeted $2x$ % values

(see Figure s4). With increasing the heat treatment temperature, the x refined values are decreasing for two reasons: 1/ because less europium cations are located into the CaFAp structure and 2/ because of the increasing amount of the secondary monazite phase. The two calcium sites behave differently with the heat treatment. The as-prepared samples present europium cation in both the Ca(1) and Ca(2) calcium site in an almost equivalent proportion (see Figure s5). The increase in the heat treatment induces the progressive departure of Eu^{3+} from the Ca(1) site; the latter is free of substitution for the 1000°C series. On the other hand, the Eu^{3+} substitution level in the Ca(2) site is not temperature dependant. The doping-emptying of the Ca(1) site explains the decrease of the x refined value with the increase of temperature. The different behaviour of the two Ca(1) and Ca(2) sites can be attributed to the two dense and low-density columns in the CaFAp structure. Dense columns are built around the Ca(1) sites in a relatively rigid organisation. Contrary, the low-density columns are built around the Ca(2) sites and they are more flexible because of the presence of fluoride anions in the Ca^{2+} neighbouring. The F^- location can be shifted (well-known in the case of hydroxyl anion in CaHAp structure) to accommodate the slight ionic radius difference between Ca^{2+} and Eu^{3+} . Three observations can be made on the variation of the coherent domain size:

- For the undoped samples, the coherent domain size is directly related to the thermal treatment. An increase of crystallinity is observed for an increase in the treatment temperature.
- The Eu-doping affects strongly the crystallinity of the sample. The coherent domain size sharply decreases as soon as small amount of europium is present.
- For the Eu^{3+} -doped samples, only the 1000°C treatment allows to induce an increase of the coherent domain size. The three as-prepared, 500°C and 800°C series show quite similar coherent domain size.

The projection of the fluorapatite unit cells, the coordination polyhedra of Ca^{2+} cations and coordination polyhedra of fluorine ions are shown in Figure 3.

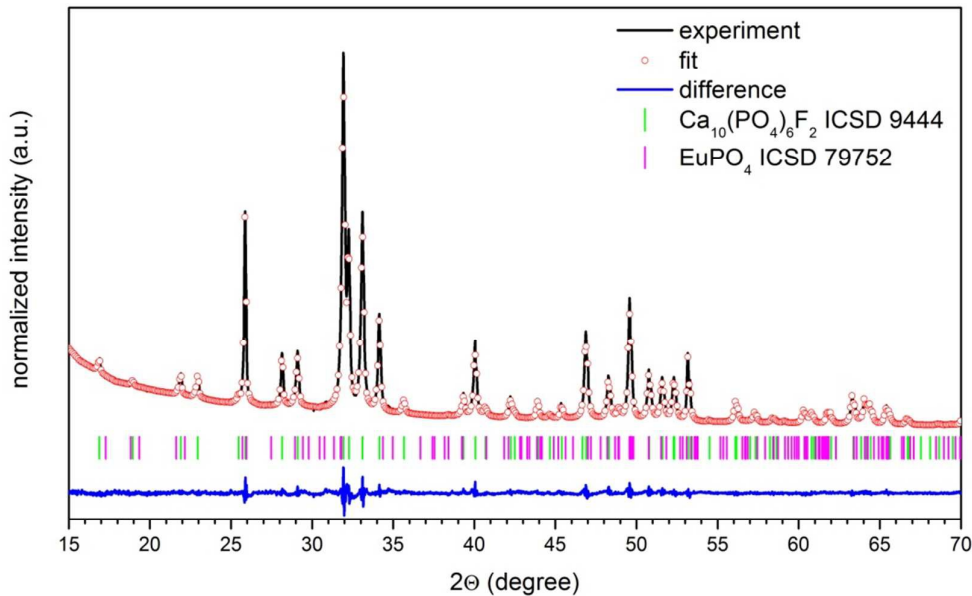


Figure 2. Representative result of the Rietveld analysis for the $\text{Ca}_{9.85}\text{Eu}_{0.1}(\text{PO}_4)_6\text{F}_2$ obtained at 500°C (red – fitted diffraction; blue – differential pattern, column – reference phase peak position).

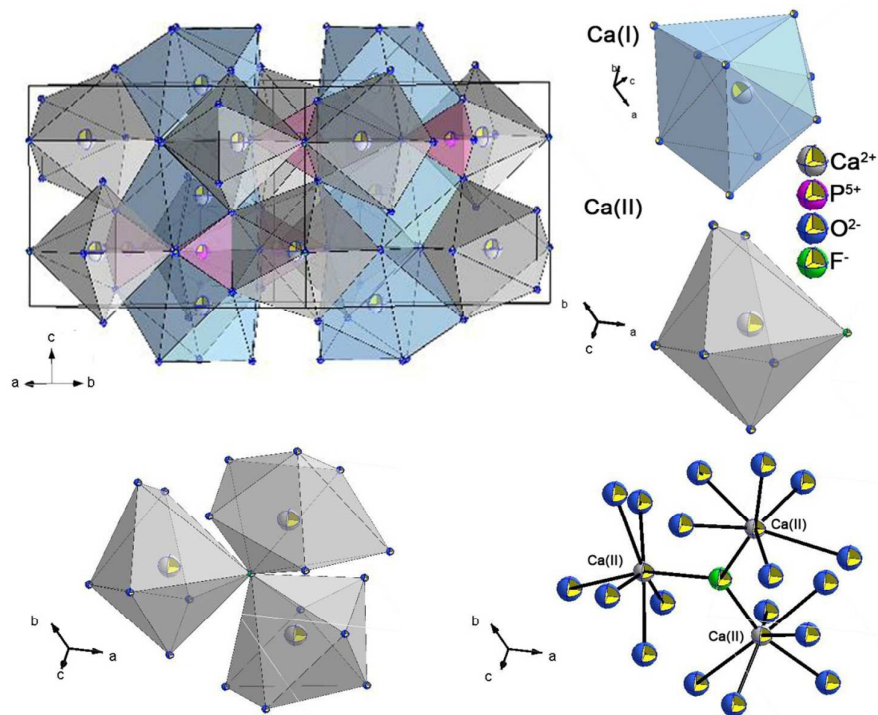


Figure 3. Projection of the $\text{Ca}_{10}(\text{PO}_4)_6\text{F}_2$ unit cell with indication of the Ca(1) and Ca(2) as well as the closest crystallographic surrounding of F^- anion (polyhedra and connectivity).

3.1.1. Calcium sites description

The calcium atoms are aligned along the hexagonal axis (forming dense column with the Ca(1) site and sparser column with the Ca(2) site) and are surrounded by phosphate groups (6 PO₄ around Ca(1) and 5 PO₄ around Ca(2)) forming channels in which are located the fluoride anions. All phosphates are equivalents (1 single P site) and oxygen atoms are described by three positions (O(1), O(2) and O(3)). The Ca(1) site is 9-fold coordinated: 3 PO₄ approaching an edge (2 oxygen atoms) and 3 PO₄ approaching a corner (1 single oxygen atom). The Ca(2) site is 7-fold coordinated (pseudo pentagonal based bipyramid): 1 PO₄ approaching an edge, 4 PO₄ approaching a corner and one fluoride neighbouring anion. The presence of the fluoride anion (which can move quite easily along the hexagonal axis) brings flexibility to this Ca(2) site which can accommodate more easily a cationic substitution mechanism.

3.1.2. IR and Raman spectra

The infrared spectra were recorded for the Ca_{9.85}Eu_{0.1}(PO₄)₆F₂ heat treated at 600°, 800°, 1000°C and the Raman spectra were recorded for the Ca_(10-3x)Eu_{2x}(PO₄)₆F₂, where 2x = 0.5, 1, 2, 3 mol% of Eu³⁺ ions, to analyse in detail structural properties of synthesised materials. The results are shown in Figures 4 and 5. In the IR spectra, characteristic active vibrational transitions of the PO₄³⁻ groups are clearly visible: the doubly degenerated ν_2 bending at 473 cm⁻¹, the triply degenerated ν_4 vibration at 562.1 and 598.3 cm⁻¹, the ν_1 non-degenerated symmetric stretching at 963.7 cm⁻¹, the triply degenerated antisymmetric stretching at 1018.7 and 1092.5 cm⁻¹³⁸. The peaks connected with vibration transitions of OH⁻ groups at about 3500 cm⁻¹ and 630 cm⁻¹ are not observed. Moreover, additional peak at 745.7 cm⁻¹ was observed that could be assigned to the F-OH-F configuration and may be transferred by one to another with relatively low energy¹². A small difference in location between particular peaks are noticeable which could be related with fluoride ions departure from fluorapatite structure after increasing the annealing temperature and therefore, with changes in internal structure of obtained materials. The Raman spectra consist of three overlapping peaks located at 1052.7, 1042.1 and 1034.4 cm⁻¹ connected with asymmetric stretching (ν_3) of the PO₄³⁻ group³⁸. These peaks are located at almost the same Raman shift which indicate that europium(III) ions concentration does not affected strongly the fluorapatite structure.

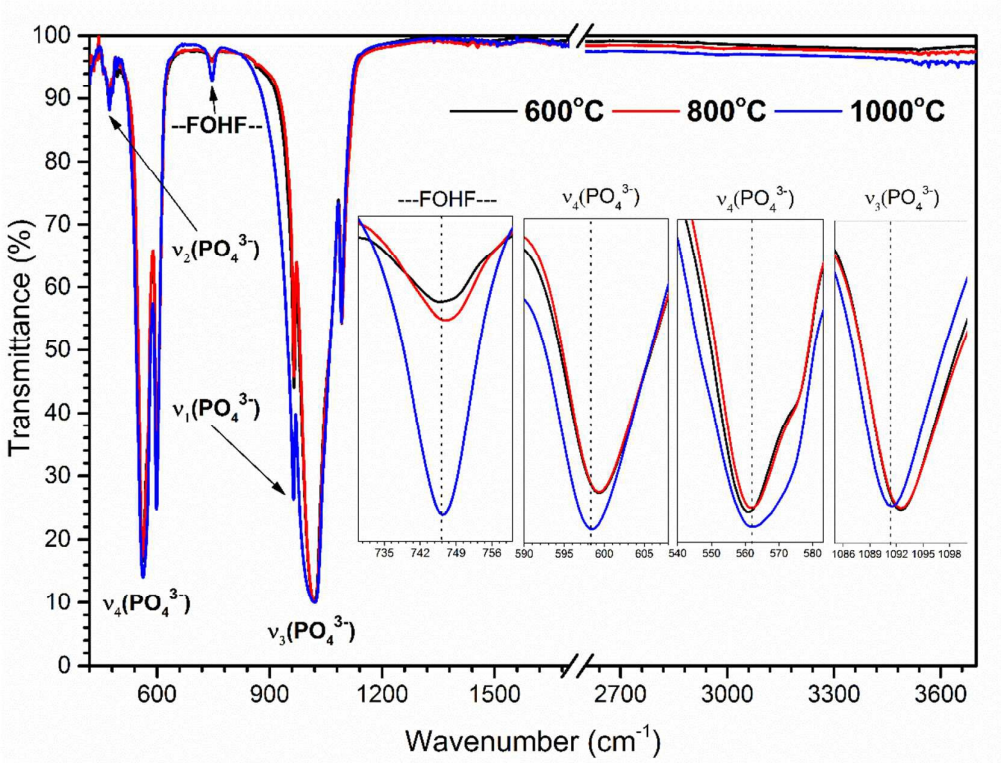


Figure 4. IR spectra of the $\text{Ca}_{9.85}\text{Eu}_{0.1}(\text{PO}_4)_6\text{F}_2$ prepared by microwave assisted hydrothermal synthesis and heat-treated at different temperatures.

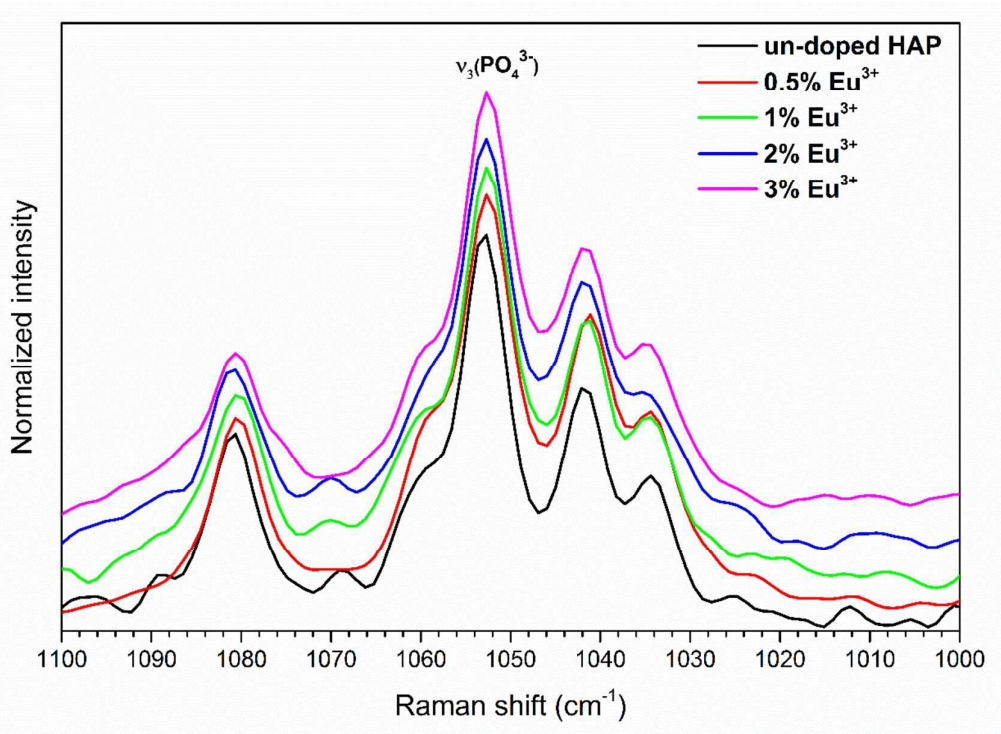


Figure 5. Raman spectra of the $\text{Ca}_{(10-3x)}\text{Eu}_{2x}(\text{PO}_4)_6\text{F}_2$ prepared by microwave assisted hydrothermal synthesis and heat-treated at 600°C/3h.

The morphology of the calcium fluorapatite doped with 1 mol% of Eu^{3+} and heat treated at 500°C was studied *via* TEM and Selected Area Electron Diffraction (SAED) techniques. As can be seen in Figure 6, nanoparticles are crystalline with a low level of aggregation. The particles are elongated in one direction and have grown up in rectangular prism nanorods. The preparation of pure phase fluorapatite was additionally confirmed by SAED analysis. Moreover, the nanoparticles of the $\text{Ca}_{9.85}\text{Eu}_{0.1}(\text{PO}_4)_6\text{F}_2$ annealed at 500°C were counted in length and width diameters according to TEM measurements that correspond very well with the Rietveld calculations.

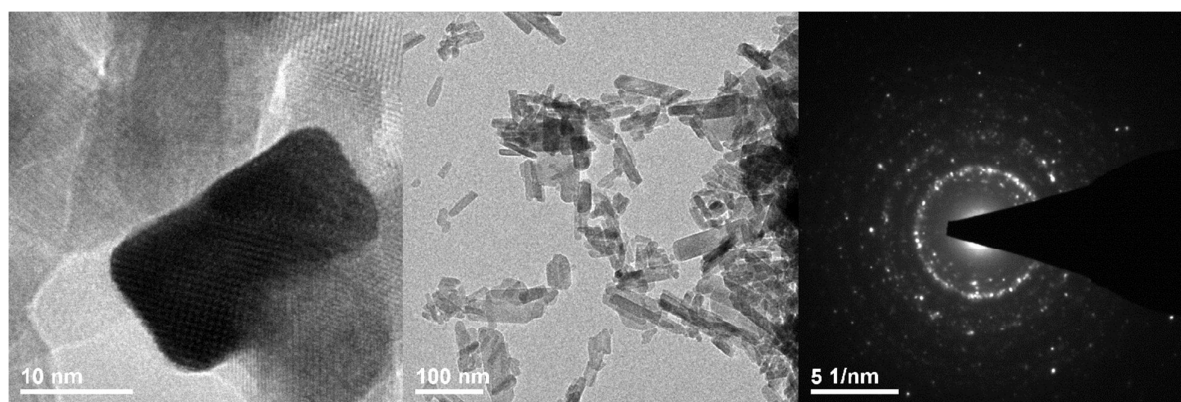


Figure 6. Representative TEM images and SAED image of the $\text{Ca}_{9.85}\text{Eu}_{0.1}(\text{PO}_4)_6\text{F}_2$ prepared by microwave stimulated hydrothermal synthesis and annealed at $500^\circ\text{C}/3\text{h}$.

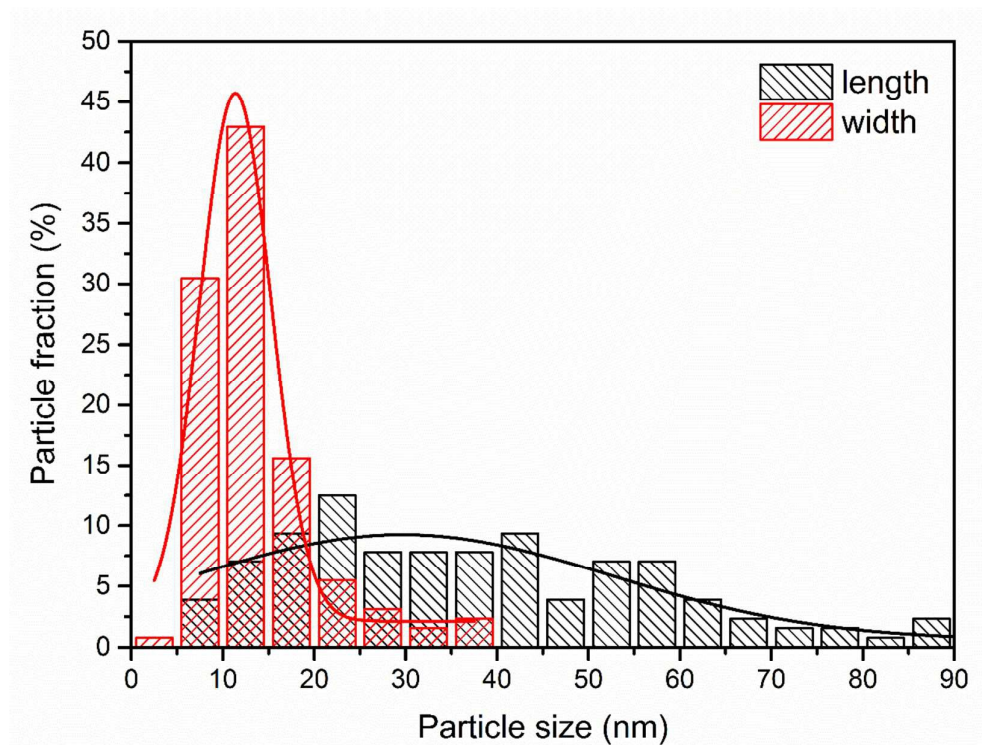


Figure 7. Histogram of the grain size distribution (length and width diameters) of the $\text{Ca}_{9.85}\text{Eu}_{0.1}(\text{PO}_4)_6\text{F}_2$ prepared by microwave stimulated hydrothermal synthesis and annealed at $500^\circ\text{C}/3\text{h}$.

3.2. Optical properties

Above terminal concentration of 3 mol% Eu^{3+} in fluorapatite lattice, phases separation were detected and appearance of extra EuPO_4 crystal phase was noticed. Because of this, only samples in the 0.5 – 3 mol% concentration range and in the $500 - 1000^\circ\text{C}$ temperature range were characterized *via* the PL emission and excitation spectra, as shown in Figures 8, 9 and 10. The representative excitation/emission spectra recorded at 618 nm emission line corresponding to the maximum intensity of the $^5D_0 \rightarrow ^7F_2$ electric dipole transition and representative emission spectra obtained under pulsed 266 nm excitation at 300 K for CaFAp doped with 1 mol% Eu^{3+} ions are presented in Figure 8. The excitation spectra consist of an allowed, strong and broad band localized in the ultraviolet range of electromagnetic radiation relative with ligand-to-metal charge transfer (C–T) $\text{Eu}^{3+} \leftrightarrow \text{O}^{2-}$ of PO_4^{3-} group as well as of series forbidden, weak and narrow lines connected with the intraconfigurational $f-f$ transitions. The maximum of CT transition is located at $40\,000\text{ cm}^{-1}$ (250 nm) and could be strongly affected by extrinsic crystal field. On the other hand, the narrow lines observed at

33 613 cm^{-1} (297 nm) were assigned to ${}^7F_0 \rightarrow {}^5F_{(4,3,2,1)}, {}^3P_0$ transitions; at 31 397 cm^{-1} (318.5 nm) to ${}^7F_0 \rightarrow {}^5H_{(6,5,4,7,3)}$; at 27 662 cm^{-1} (361.5 nm) to ${}^7F_0 \rightarrow {}^5D_4$; at 26 178 cm^{-1} (382 nm) to ${}^5L_8, {}^7F_0 \rightarrow {}^5G_{(2,3)}, {}^5L_7$; at 25 381 cm^{-1} (394 nm) to ${}^7F_0 \rightarrow {}^5L_6$; at 21 528 cm^{-1} (464.5 nm) to ${}^7F_0 \rightarrow {}^5D_2$; at 18 762 cm^{-1} (533 nm) to ${}^7F_0 \rightarrow {}^5D_1$ and at 16 949 cm^{-1} (590 nm) to ${}^7F_0 \rightarrow {}^5D_0$. The positions of maxima of $f-f$ transitions are independent on the host lattice structure and remains almost constant due to a good isolation of the f shells by the external orbitals as well as low electron-lattice coupling^{19,26}.

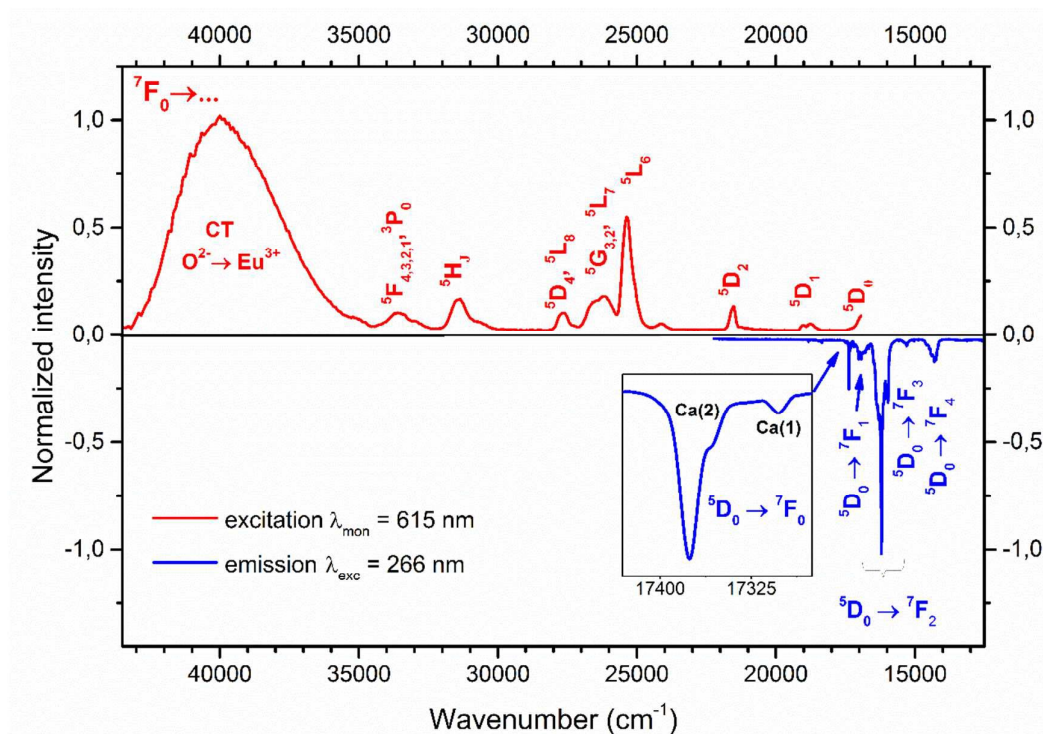


Figure 8. Representative excitation spectra (red line) and emission spectra (blue line) of the $\text{Ca}_{9.85}\text{Eu}_{0.1}(\text{PO}_4)_6\text{F}_2$ nanoparticles annealed at 800°C.

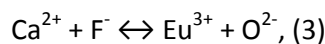
The room-temperature emission spectra of the $\text{Ca}_{(10-3x)}\text{Eu}_{2x}(\text{PO}_4)_6\text{F}_2$ nanopowders were acquired in the spectral range from 17 500 nm to 14 000 cm^{-1} under pulsed 266 nm excitation as a function of optically active ions concentrations ($2x = 0.5 - 3$ mol%) for three calcination temperatures (600°, 800°, 1000°C) and as a function of annealing temperature (as-prepared - 1000°C). All the spectra were normalized to the ${}^5D_0 \rightarrow {}^7F_1$ magnetic dipole transition due to low dependence of host lattice to its intensity^{39,40} (see Figure 9). As can be seen, classic emission spectra of Eu^{3+} ions consisting of five peaks located nearly 17 343 cm^{-1} (576 nm), 16 903 cm^{-1} (591.6 nm), 16 174 cm^{-1} (618 nm), 15 276 cm^{-1} (654.6 nm) and 14 313 cm^{-1} (699 nm) can be observed. These peaks are related with $f-f$ transitions inside the f shell

of Eu^{3+} ions: $^5D_0 \rightarrow ^7F_0$, $^5D_0 \rightarrow ^7F_1$, $^5D_0 \rightarrow ^7F_2$, $^5D_0 \rightarrow ^7F_3$ and $^5D_0 \rightarrow ^7F_4$ respectively. The most efficient emission was observed for the hypersensitive $^5D_0 \rightarrow ^7F_2$ electron transition. The europium ion is often used as a structural and luminescence probe owing to its sensitivity to the even slight changes in its local surrounding. To accomplish this target, the $^5D_0 \rightarrow ^7F_{0,1,2}$ transitions were analyzed. Since, the 7F_0 ground state and the 5D_0 first excited state are non-degenerated under any symmetry, study of the $^7F_0 - ^5D_0$ transition can give straightforward information about the existence of the total crystallographic sites substituted by europium(III) ions in the matrix. Moreover, the presence of this transition confirms the low symmetry environment of the Eu^{3+} built into the host lattice¹⁹. The $^5D_0 \rightarrow ^7F_2$ electric dipole transition is enormously sensitive even to minor changes in the local environment of the Eu^{3+} ions whereas the $^5D_0 \rightarrow ^7F_1$ magnetic dipole transition remains nearly independent on the symmetry and matrix. In this matter, the magnetic dipole transition can be considered as an internal reference. If the Eu^{3+} ion is in position with the center of symmetry, only the magnetic transition is permitted. On the other hand, the electric dipole transition is dominant^{39–41}. The relative emission intensities ratio (R) is defined as follows:

$$R = \frac{\int ^5D_0 \rightarrow ^7F_2}{\int ^5D_0 \rightarrow ^7F_1}, \quad (2)$$

Through this simple equation it is possible to notice little changes in the local environment of Eu^{3+} ions. The ratio between integral intensity of these transitions is used for the assessment of the europium(III) ions coordination polyhedron asymmetry. This entails that the bigger the ratio between these transitions, the less centrosymmetric local surrounding around Eu^{3+} is. The influence of calcination temperature and Eu^{3+} ions concentration on R value is presented in Table 2.

Considering the crystallographic data of calcium fluorapatite, Eu^{3+} dopant can theoretically be incorporated at both Ca(1) and Ca(2) crystallographic positions. The Ca(1) position with C_3 symmetry is coordinated by nine oxygen ions of PO_4^{3-} group and the Ca(2) position with C_s symmetry is coordinated by six oxygen ions of PO_4^{3-} group and one fluorine ion. It is worth to emphasize that only Ca^{2+} ions located at C_s crystallographic site is directly bonded with fluorine ion and one fluorine ion is surrounded by three Ca(2) ions (see Figure 3). The substitution of europium(III) ions into calcium sites needs a charge compensation mechanism, describes as^{16,17}:



or



The first mechanism seems to be more probable for apatite and it is possible only for Ca(2) site in C_s symmetry, because only this ions is surrounded by one fluorine atom, which could be easily substituted during wet synthesis by oxygen ion coming from water. The second mechanism can lead to substitution of two Ca(2) ions which belongs to the same triangle built from calcium ions or to different triangles known as *cis*-symmetry and *trans*-symmetry arrangements of substituted Eu^{3+} ions along the channel structures from these triangles. In the literature it is well-known that three lines for the $0-0$ transition are present in apatite compounds^{42,43}.

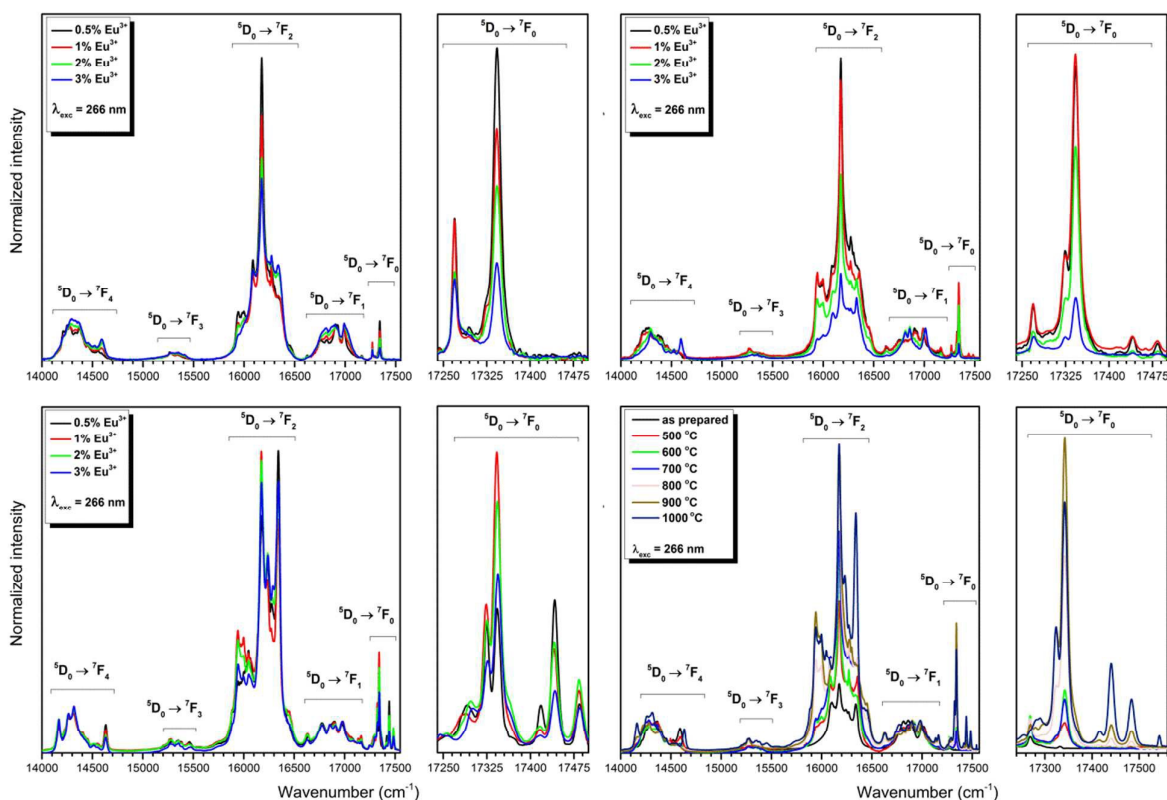


Figure 9. Emission spectra of the $\text{Ca}_{(10-3x)}\text{Eu}_{2x}(\text{PO}_4)_6\text{F}_2$ nanoparticles annealed at 600°C (left upper), 800°C (right upper), 1000°C (left bottom) and the $\text{Ca}_{9.85}\text{Eu}_{0.1}(\text{PO}_4)_6\text{F}_2$ depending on annealed temperature (right bottom).

Taking into account the CaFap:Eu^{3+} calcined at 600°C/3h (see Figure 9), the $^5\text{D}_0 \rightarrow ^7\text{F}_0$ transition consists of two maxima located at $17\,343\text{ cm}^{-1}$ (576.6 nm – Ca(2) site with C_s

symmetry) and $17\,269\text{ cm}^{-1}$ (579.1 nm – Ca(1) site with C_3 symmetry), which corresponds well with two possibilities of europium(III) ions substitution into fluorapatite matrix. The intensity of the $^5D_0 \rightarrow ^7F_2$ transition in the ratio to the $^5D_0 \rightarrow ^7F_1$ is decreasing with increase of lanthanide ions concentration, which means the drop of distortion of europium polyhedra in the host lattice (see Table 2). The charge and ionic radii incompatibility between calcium(II) and europium(III) ions is sufficient (Ca^{2+} (CN₉) – 1.18 Å, Eu^{3+} (CN₉) – 1.12 Å, Ca^{2+} (CN₇) – 1.06 Å, Eu^{3+} (CN₇) – 1.01 Å)³⁷, but it could be compensated by escaping of fluorine ions caused by high temperature treatment. It is clearly visible that with increase of europium(III) ions concentration, the emission intensity from C_s symmetry is decreasing. In crystal lattice, the fluorine vacancies are created and the surrounding of Eu^{3+} ions is changed, hence the appearance of extra $O-O$ lines could also be related with formation of new crystal sites. In pursuance of the $2J + 1$ principle, a maximum of three sublevels should exist at C_s symmetry for the $^5D_0 \rightarrow ^7F_1$ transition and five in the case of the $^5D_0 \rightarrow ^7F_2$ transition. Whereas, a maximum of two Stark components should be present at C_3 symmetry for $^5D_0 \rightarrow ^7F_1$ and three for $^5D_0 \rightarrow ^7F_2$ transition¹⁶.

In the case of CaFAp:Eu^{3+} annealed at $800^\circ\text{C}/3\text{h}$, it is possible to distinguish five $^5D_0 \rightarrow ^7F_0$ lines located at $17\,484\text{ cm}^{-1}$ (571.9 nm), $17\,441\text{ cm}^{-1}$ (573.4 nm), $17\,342\text{ cm}^{-1}$ (576.6 nm), $17\,324\text{ cm}^{-1}$ (577.2 nm) and $17\,269\text{ cm}^{-1}$ (579.1 nm). It could be related with phase separation under high temperature treatment to extra EuPO_4 phase. Furthermore, the $O-O$ transition of Eu^{3+} ions demonstrated abnormal strong intensity (800° , 1000°C), which was connected with rising of covalent nature of the Eu-O bonding known in apatites⁴⁴.

The case of materials annealed at $1000^\circ\text{C}/3\text{h}$ is very similar to samples heat treated at $800^\circ\text{C}/3\text{h}$, but one can favour extra transitions located at $17\,291\text{ cm}^{-1}$ (578.3 nm), $17\,323\text{ cm}^{-1}$ (577.3 nm), $17\,342\text{ cm}^{-1}$ (576.6 nm), $17\,418\text{ cm}^{-1}$ (574.1 nm), $17\,442\text{ cm}^{-1}$ (573.3), $17\,484\text{ cm}^{-1}$ (572 nm). With increasing of annealing temperature, a higher amount of fluorine ions was removed enabling a creation of an extra $\text{Ca}_3(\text{PO}_4)_2$ phase with five available crystallographic sites for Eu^{3+} (see Figure s1). Thereupon, the new $O-O$ transitions were appearing. The asymmetry parameter R dropped progressively with an increase of europium(III) ions concentration for samples heat-treated at 800°C . Thereby, the local environment of Eu^{3+} got less distorted with increase of optical ions concentration. Inverse situation was observed in the case of 1000°C . The R value increased with an increase of heat-treatment temperature, that means an increase of the distortion of europium polyhedra.

Nevertheless, temperature dependent emission of the CaFAp:1% Eu^{3+} is the most interesting result. For as-prepared sample one can observe only two $0-0$ lines and the transition of Eu^{3+} located at C_3 position was more intense than at C_s crystallographic site. But in the case of sample heat-treated at $500^\circ\text{C}/3\text{h}$, the intensity of both $0-0$ transitions was almost identical. After further elevating the annealing temperature to $600^\circ\text{C}/3\text{h}$ and to $700^\circ\text{C}/3\text{h}$, the most intense $0-0$ transition was observed from C_s symmetry of Eu^{3+} ions into fluorapatite structure. In samples annealed at $800^\circ\text{C}/3\text{h}$, $900^\circ\text{C}/3\text{h}$ and $1000^\circ\text{C}/3\text{h}$, one can observe five $0-0$ lines and the most intense line comes from radiative transition of Eu^{3+} ions located at C_s symmetry. This behavior is well known in the literature and is connected with thermal diffusion of europium ions^{45,46}. The R value was increasing with increase of annealing temperature from 1.96 for as-prepared material to 6.04 for material heat treated at 1000°C (see Table 1). Moreover, it was demonstrated that the fraction of the $^5D_0 \rightarrow ^7F_4$ transition with respect to the whole emission spectrum decrease with increasing of annealing temperatures. The electronegativity of the Eu^{3+} cations does not change due to the same concentration of Eu^{3+} in samples annealed at different temperatures⁴⁷. However, it can be seen significant increasing in the intensity of the $^5D_0 \rightarrow ^7F_2$, so-called “hypersensitive transition” that leads to the conclusion that the local symmetry of the Eu^{3+} ion in fluorapatites get more distorted with increasing of heat-treatment temperature.

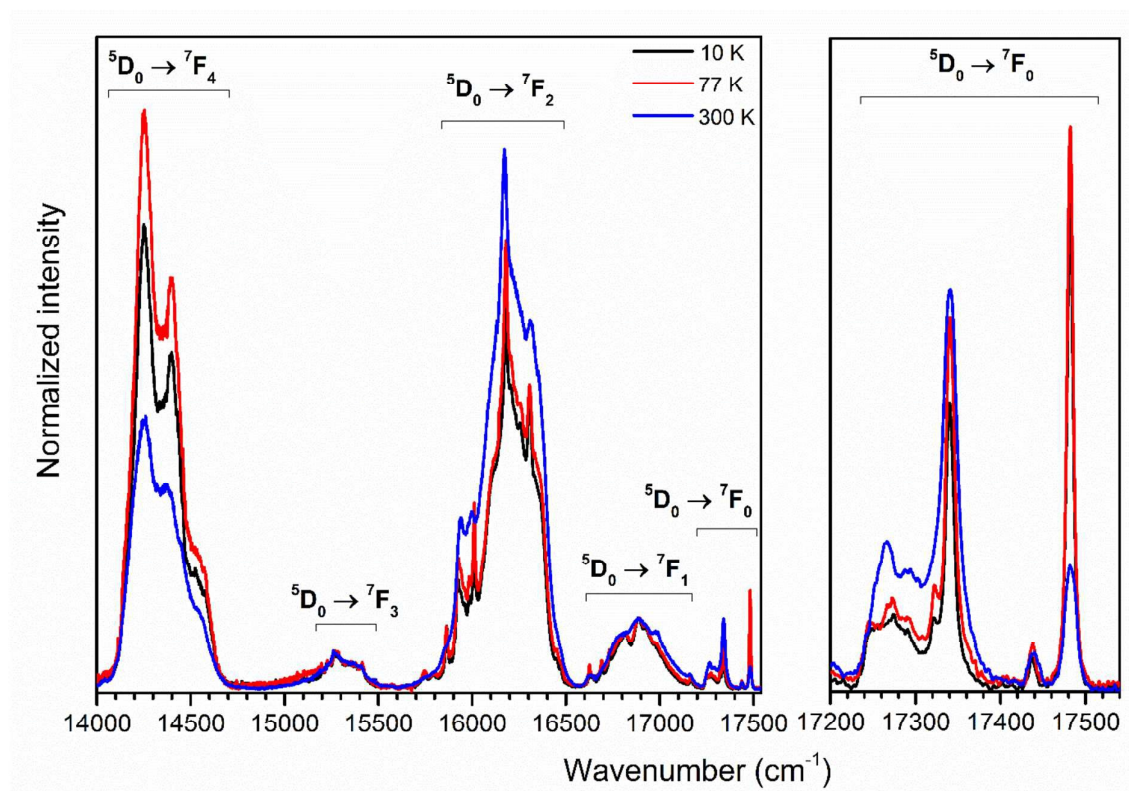


Figure 10. Representative emission spectra of the $\text{Ca}_{9.85}\text{Eu}_{0.1}(\text{PO}_4)_6\text{F}_2$ nanoparticles annealed 800°C measured at different temperatures.

In order to get deeper insight into fluorapatite structure, emission spectra of the $\text{Ca}_{9.85}\text{Eu}_{0.1}(\text{PO}_4)_6\text{F}_2$ annealed at 600° and 800°C per 3 h were measured at three different temperatures (10, 77 and 300 K, see Figure 10). All emission spectra were normalized to the $^5\text{D}_0 \rightarrow ^7\text{F}_1$ transition. As can be clearly seen, it is easier to isolate particular Stark components at 10 K than at higher temperature of measurement. It is visible that with decreasing of measurement temperature the intensity of electric dipole transition was decreasing. It is possible to distinguish four *O-O* lines located at $17\,266\text{ cm}^{-1}$ (579.2 nm), $17\,341\text{ cm}^{-1}$ (576.7 nm) and $17\,438\text{ cm}^{-1}$ (573.5 nm) and $17\,482\text{ cm}^{-1}$ (572 nm) for all measurement temperatures. An extra *O-O* line was observed, what could be connected with creation of additional EuPO_4 phase as well as with departure of fluorine ions and creation of different Eu^{3+} surrounding.

The simplified Judd-Ofelt theory was used to determine the Ω_2 and Ω_4 intensity parameters based on proceeding given in references^{19,48,49}. Calculations were collected in Table 2. The value of the Ω_2 parameter decreases while increasing the Eu^{3+} ions concentration for materials heat-treated at 600°C and 800°C , whereas it remains

unpredictable for materials at 1000°C. The Ω_2 value increases with increasing of heat-treatment temperature. The R parameter change yields almost the same trend as Ω_2 and also indicates the rise of distortion of europium polyhedra as well as it could be related with increase of the $\text{Eu}^{3+}\text{-O}^{2-}$ bond covalency. The Ω_4 parameter can deliver some information about changes in the electron density around Eu^{3+} ions. The magnitude of this parameter falls with increase of europium(III) ions concentration for sample annealing at 600°C until 2 mol% then decreases. In the case of sample annealed at 800°C and 1000°C, this parameter behaves variously. The Ω_4 value increases with increase of heat-treatment temperature until 700 °C and then decreases excepted of sample annealed at 1000°C. Moreover, the changes in the ${}^5D_0 \rightarrow {}^7F_2/{}^5D_0 \rightarrow {}^7F_4$ ratio with increasing of annealing temperature are caused by deformation of the fluorapatite structure as well as perturbation of the Eu^{3+} sites in the matrix. The high intensity of the ${}^5D_0 \rightarrow {}^7F_4$ transition is a consequence of increasing of Ω_4 parameters connected with covalence of Eu-O bonding in a highly polarized chemical environment made by the geometric distortion of the europium polyhedron. It leads to an increase in the intensity of the ${}^5D_0 \rightarrow {}^7F_0$ and the ${}^5D_0 \rightarrow {}^7F_4$ transitions in the emission spectrum, in contrast to the ${}^5D_0 \rightarrow {}^7F_2$ transition. The general trend in theoretical Quantum Efficiency (QE) was observed that this parameter is decreasing with increase of europium(III) ions concentration. The highest values of QE are observed for the CaFAp doped with 0.5 mol% Eu^{3+} annealed at 600 °C (~90%) and for the CaFAp doped with 1 mol% Eu^{3+} heat-treated at 700°C (~93%). These materials are the most suitable for bioapplications due to nanometric size as well as good luminescence properties.

Table 2. Decay rates of radiative (A_{rad}), non-radiative (A_{nrad}) and total (A_{tot}) processes of ${}^5D_0 \rightarrow {}^7F_J$ transitions, emission lifetimes (τ), intensity parameters (Ω_2 , Ω_4), quantum efficiency (η) and asymmetry ratio (R) of the $\text{Ca}_{(10-3x)}\text{Eu}_{2x}(\text{PO}_4)_6\text{F}_2$ as function of Eu^{3+} concentration and calcination temperature.

Sample		A_{rad} (s^{-1})	A_{nrad} (s^{-1})	A_{tot} (s^{-1})	T (ms)	Ω_2 (10^{-20} cm^2)	Ω_4 (10^{-20} cm^2)	η (%)	R
600°C	0.5 %	292.66	31.28	323.94	3.087	7.6565	3.7601	90.34	5.44
	1 %	246.59	80.85	327.44	3.054	6.0414	3.5812	75.31	4.29
	2 %	236.46	133.22	369.69	2.705	5.7255	3.4604	63.96	4.07
	3 %	222.24	125.83	348.07	2.873	5.1347	3.5978	63.85	3.65
800°C	0.5 %	297.56	56.30	353.86	2.826	8.2046	2.9921	84.09	5.83
	1 %	272.26	70.67	342.93	2.916	7.3899	2.7434	79.39	5.25

	2 %	238.02	150.18	388.20	2.576	6.0441	2.9143	61.31	4.29
	3 %	182.02	180.43	362.45	2.759	4.0259	2.8119	50.22	2.86
1000°C	0.5 %	304.81	209.85	514.67	1.943	8.4739	2.9889	59.22	6.02
	1 %	304.27	264.88	569.15	1.757	8.5000	2.8924	53.46	6.04
	2 %	313.63	218.00	531.63	1.881	8.8397	2.9045	58.99	6.28
	3 %	321.13	184.43	505.56	2.030	9.1582	2.8178	63.52	6.50
1% Eu ³⁺	as-	152.33	213.17	365.50	2.736	2.7658	3.1550	41.68	1.96
	500°	207.59	129.45	337.04	2.967	4.7683	3.2340	61.59	3.39
	600°	246.59	80.85	327.44	3.054	6.0414	3.5812	75.31	4.29
	700°	283.29	19.74	303.03	3.300	7.2815	3.8205	93.48	5.17
	800°	272.26	70.67	342.94	2.916	7.3898	2.7434	79.39	5.25
	900°	290.36	140.67	431.03	2.320	8.1024	2.6503	67.36	5.75
	1000°	304.27	264.88	569.15	1.757	8.5000	2.8924	53.46	6.04

3.3. Decay times

The luminescence kinetics were recorded at room temperature for obtained samples in the 0.5 – 3 mol% concentration range as a function of the dopant concentration and in the 500 – 1000°C temperature range as a function of the annealing temperature corresponding to the ⁵D₀ → ⁷F₂ transition excited by 266 nm and monitored at 618 nm. The collected luminescence decay curves normalized to the signal intensity are shown in Figure 11. Since, the decay profiles are not a single exponential and an explanation of the physical meaning of the multi-exponential fitting is complicated, the value of lifetimes were calculated as the effective emission decays using the following equation:

$$\tau_m = \frac{\int_0^\infty tI(t)dt}{\int_0^\infty I(t)dt} \cong \frac{\int_0^{t^{max}} tI(t)dt}{\int_0^{t^{max}} I(t)dt}, (5)$$

where *I(t)* is the luminescence intensity at time *t* corrected for the background and the integrals are evaluated on a range 0 < *t* < *t*^{max}, where *t*^{max} >> τ_{*m*}.

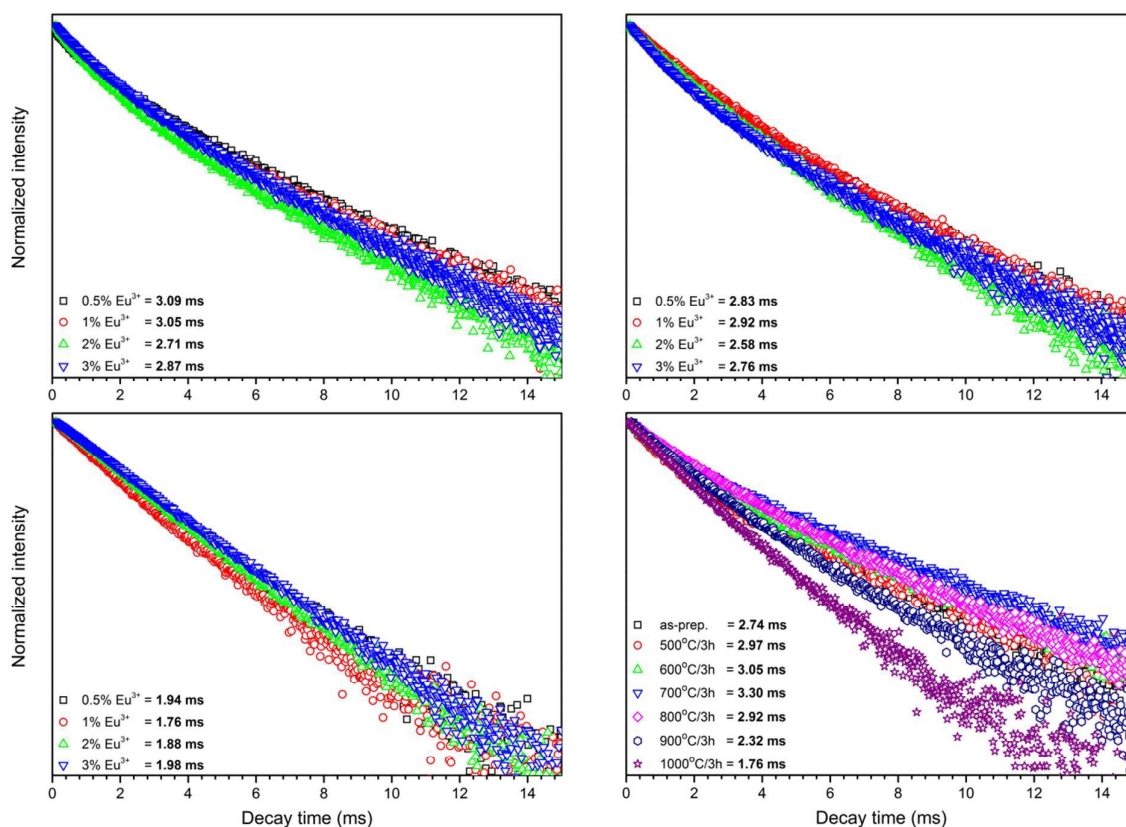


Figure 11. Luminescence decay profiles of annealed at 600°C (left upper), 800°C (right upper), 1000°C (left bottom) and the $\text{Ca}_{9.85}\text{Eu}_{0.1}(\text{PO}_4)_6\text{F}_2$ depending on annealed temperature (right bottom).

The decay profiles and the lifetime values of materials annealed at 600°C are all similar around 3 ms. Slight changes observed between values are within the margin of error (5% of decay time value). The lifetime values of samples annealed at 800°C and 1000°C are around 2.8 ms and 1.9 ms, respectively and they behave in similar way to the above case. In the case of the CaFAp doped with 1 mol% Eu^{3+} and heat treated at different temperatures, firstly average decay time increased while increasing the temperature from 2.7 ms for as-prepared sample to 3.3 ms for sample calcinated at 700°C. Then, the average lifetime decreases down to 1.8 ms for sample calcinated at 1000°C. If one carefully compares these results with emission spectra, one can notice that with increase of annealing temperature, the intensity of the $0-0$ line of Eu^{3+} in C_s symmetry increases and results in an increase of the lifetime. But this is observed only below 700°C, then despite increasing of the $0-0$ line intensity of Eu^{3+} in C_s site, the decay time decreased. It could be connected with preferential building of Eu^{3+} ions into C_s symmetry than C_3 symmetry with increase of heat-treatment temperature (see Figure 9) as a result of thermal diffusion of Eu^{3+} ions.

The fluorapatites possess defects in crystal structure created by dopant and departure of fluorine ions caused by heat-treatment. This could be responsible for the overall lifetime of Eu^{3+} ion due to the contribution of the increasing non-radiative process.

4. Conclusions

The aim of this work was to study the structural and luminescence properties of the $\text{Ca}_{(10-3x)}\text{Eu}_{2x}(\text{PO}_4)_6\text{F}_2$ doped with Eu^{3+} ions ($2x = 0.5 - 3$ mol%) obtained by microwave stimulated method and post heat-treated at temperature range from 500 to 1000°C per 3 h. The successful substitution of Eu^{3+} ions into fluorapatite in entire concentration scope as well as hexagonal structure of prepared materials were confirmed by the powder XRD technique. At upper terminal Eu^{3+} ions concentration, the extra EuPO_4 appeared due to charge and ionic radii incompatibility between Ca^{2+} and Eu^{3+} ions. The nanometric size of the fluorapatite activated by Eu^{3+} ions was confirmed by Rietveld refinement and TEM microscopy for all samples heat treated below 1000°C. The structural and spectroscopic properties have shown that optically active dopant were incorporated into both calcium crystallographic sites. Three *O-O* lines are visible on emission spectra derived from Eu(1) site as well as from *cis*- and *trans*-symmetry of Eu(2) site. Additional *O-O* peaks could be related with phase separation and with escaping of fluorine ions influenced by high annealing temperature. The highly intense *O-O* transitions were observed for materials heat treated above 800°C which was connected with an increase of covalent character of Eu-O bonding.

5. Acknowledgements

This work was supported by the National Science Centre project titled 'Nanomaterials for fluorescence lifetimes bio-imaging (NFLBio)' (no. UMO-2012/06/M/ST5/00048). The authors are grateful for the help with XRD measurements to M.Sc. E. Bukowska, for TEM images to Ph.D. M. Malecka and for IR and Raman measurements to M.Sc. A. Ciupa as well as Ph.D. L. Marciniak and Ph.D. R. Pazik for help with spectroscopic measurements.

6. References

- 1 P. Layrolle and A. Lebugle, *Chem. Mater.*, 1996, **8**, 134–144.
- 2 A. Yasukawa, K. Kandori, H. Tanaka and K. Gotoh, *Mater. Res. Bull.*, 2012, **47**, 1257–1263.
- 3 S. Pratheep Kumar and G. Buvaneswari, *Mater. Res. Bull.*, 2013, **48**, 324–332.
- 4 M. H. Fathi, A. Hanifi and V. Mortazavi, *J. Mater. Process. Technol.*, 2008, **202**, 536–542.
- 5 M. V Chaikina, I. A. Khlosov, A. V Karlov and K. S. Paichadze, *Chem. Sustain. Dev.*, 2004, **12**, 385–394.
- 6 P. Ducheyne and Q. Qiu, *Biomaterials*, 1999, **20**, 2287–2303.
- 7 A. Hanifi and M. H. Fathi, *Iran. J. Pharm. Sci.*, 2008, **4(2)**, 141–148.
- 8 N. Senamaud, D. Bernache-Assollant, E. Champion, M. Heughebaert and C. Rey, *Solid State Ionics*, 1997, **101–103**, 1357–1362.
- 9 R. J. Wiglusz, B. Pozniak, K. Zawisza and R. Pazik, *RSC Adv.*, 2015, **5**, 27610–27622.
- 10 M. Nabyouni, H. Zhou, T. J. F. Luchini and S. B. Bhaduri, *Mater. Sci. Eng. C*, 2014, **37**, 363–368.
- 11 J. Zhao, X. Dong, M. Bian, J. Zhao, Y. Zhang, Y. Sun, J. Chen and X. Wang, *Appl. Surf. Sci.*, 2014, **314**, 1026–1033.
- 12 A. Bianco, I. Cacciotti, M. Lombardi, L. Montanaro, E. Bemporad and M. Sebastiani, *Ceram. Int.*, 2010, **36**, 313–322.
- 13 M. Sheykhani, A. Heydari, L. Ma'mani and A. Badiei, *Spectrochim. Acta - Part A Mol. Biomol. Spectrosc.*, 2011, **83**, 379–383.
- 14 L. M. Rodríguez-Lorenzo, J. N. Hart and K. A. Gross, *Biomaterials*, 2003, **24**, 3777–3785.
- 15 H. Wang, K. Sun, A. Li, W. Wang and P. Chui, *Powder Technol.*, 2011, **209**, 9–14.
- 16 M. Karbowiak and S. Hubert, *J. Alloys Compd.*, 2000, **302**, 87–93.
- 17 R. Sahoo, S. K. Bhattacharya and R. Debnath, *J. Solid State Chem.*, 2003, **175**, 218–225.
- 18 X. Li, J. Zhu, Z. Man, Y. Ao and H. Chen, *Sci. Rep.*, 2014, **4**, 4446.
- 19 R. Pazik, J.-M. Nedelec and R. J. Wiglusz, *CrystEngComm*, 2014, **16**, 5308–5318.
- 20 X. X. Zhang, G. B. Loutts, M. Bass and B. H. T. Chai, *Appl. Phys. Lett.*, 1994, **64**, 10–12.
- 21 J. Akiyama, Y. Sato and T. Taira, *Appl. Phys. Express*, 2011, **4**, 22703.
- 22 J. B. Gruber, C. A. Morrison, M. D. Seltzer, A. O. Wright, M. P. Nadler, T. H. Allik, J. A. Hutchinson and B. H. T. Chai, *J. Appl. Phys.*, 1996, **79**, 1746–1758.
- 23 A. O. Wright, M. D. Seltzer, J. B. Gruber, B. Zandi, L. D. Merkle and B. H. T. Chai, *J. Phys. Chem. Solids*, 1996, **57**, 1337–1350.
- 24 C. E. Bonner, P. M. Mwangi, S. J. Creekmore, L. J. Richardson, S. Stefanos, G. B. Loutts and B. Walsh, *Opt. Mater. (Amst.)*, 2002, **20**, 1–12.
- 25 Y. Sun, H. Yang and D. Tao, *Ceram. Int.*, 2012, **38**, 6937–6941.
- 26 P. Sobierajska, R. Pazik, K. Zawisza, G. Renaudin, J.-M. Nedelec and R. J. Wiglusz, *CrystEngComm*, 2016, **18**, 3447–3455.
- 27 X. Hu, J. Zhu, X. Li, X. Zhang, Q. Meng, L. Yuan, J. Zhang, X. Fu, X. Duan, H. Chen and Y. Ao, *Biomaterials*, 2015, **52**, 441–51.
- 28 P. Sobierajska, K. Zawisza, R. M. Kowalski, G. Renaudin, J.-M. Nedelec, J. Zienkiewicz and R. J. Wiglusz, *RSC Adv.*, 2017, **7**, 30086–30095.
- 29 J. Rodriguez-Carvajal, *Multi-pattern Rietveld Refinement program Fullprof. 2k, version 3.30*, Laboratoire Léon Brillouin, CEA Saclay: Gif-sur-Yvette, France, June 2005.
- 30 L. Lutterotti, S. Matthies and H.-R. Wenk, *IUCr Newsl. CPD*, 1999, **21**, 14–15.
- 31 L. B. McCusker, R. B. Von Dreele, D. E. Cox, D. Louer and P. Scardi, *J. Appl. Crystallogr.*, 1999, **32**, 36–50.
- 32 R. J. Hill, *J. Appl.*, 1992, **25**, 589–610.
- 33 K. Sudarsanan, P. E. Mackie and R. A. Young, *Mater. Res. Bull.*, 1972, **7**, 1331–1338.
- 34 Y. Ni, J. M. Hughes and A. N. Mariano, *Am. Mineral.*, 1995, **80**, 21–26.
- 35 K. K. Palkina, N. E. Kuz'mina, B. F. Dzhurinskii and E. G. Tselebrovskaya, *Dokl Akad Nauk*, 1995, **341(5)**, 644–648.
- 36 E. Balan, S. Delattre, D. Roche, L. Segalen, G. Morin, M. Guillaumet, M. Blanchard, M. Lazzeri, C. Brouder and E. K. H. Salje, *Phys Chem Miner.*, 2011, **38**, 111–122.
- 37 R. D. Shannon, *Acta Crystallogr.*, 1976, **A32**, 751–767.
- 38 M. Turkoz, A. O. Atilla and Z. Evis, *Ceram. Int.*, 2013, **39**, 8925–8931.
- 39 X. Huang, B. Li and H. Guo, *Ceram. Int.*, 2017, **43**, 10566–10571.

- 40 X. Huang, B. Li, H. Guo and D. Chen, *Dye. Pigment.*, 2017, **143**, 86–94.
- 41 X. Huang, H. Guo and B. Li, *J. Alloys Compd.*, 2017, **720**, 29–38.
- 42 R. Ternane, G. Panczer, M. T. Cohen-Adad, C. Goutaudier, G. Boulon, N. Kbir-Ariguib and M. Trabelsi-Ayedi, *Opt. Mater. (Amst.)*, 2001, **16**, 291–300.
- 43 R. Ternane, M. Trabelsi-Ayedi, N. Kbir-Ariguib and B. Piriou, *J. Lumin.*, 1999, **81**, 165–170.
- 44 M. Long, F. Hong, W. Li, F. Li, H. Zhao, Y. Lv, H. Li, F. Hu, L. Sun, C. Yan and Z. Wei, *J. Lumin.*, 2008, **128**, 428–436.
- 45 F. R. O. Silva, N. B. de Lima, A. H. A. Bressiani, L. C. Courrol and L. Gomes, *Opt. Mater. (Amst.)*, 2015, **47**, 135–142.
- 46 K. Zawisza and R. J. Wiglusz, *Dalt. Trans.*, 2017, **46**, 3265–3275.
- 47 R. Skaudzius, A. Katelnikovas, D. Ensling, A. Kareiva and T. Jüstel, *J. Lumin.*, 2014, **147**, 290–294.
- 48 B. Tian, B. Chen, Y. Tian, X. Li, J. Zhang, J. Sun, H. Zhong, L. Cheng, S. Fu, H. Zhong, Y. Wang, X. Zhang, H. Xia and R. Hua, *J. Mater. Chem. C*, 2013, **1**, 2338–2344.
- 49 Y. Tian, B. Chen, R. Hua, J. Sun, L. Cheng, H. Zhong, X. Li, J. Zhang, Y. Zheng, T. Yu, L. Huang and H. Yu, *J. Appl. Phys.*, 2011, **109**, 53511.